High-performance Photodetector Based on InSe/$Cs_2XI_2Cl_2$ ($X = $ Pb, Sn, and Ge) Heterostructures

Yu-Feng Ding,[1] Zhuo-Liang Yu,[1] Peng-Bin He,[1] Qiang Wan,[1] Biao Liu,[2] Jun-Liang Yang,[2] and Meng-Qiu Cai[1,*]

[1] *Key Laboratory for Micro/Nano Optoelectronic Devices of Ministry of Education & Hunan Provincial Key Laboratory of Low-Dimensional Structural Physics and Devices, School of Physics and Electronics, Hunan University, Changsha 410082, China*

[2] *Hunan Key Laboratory for Super-microstructure and Ultrafast Process, School of Physics and Electronics, Central South University, Changsha 410083, Hunan, China*

(Received 31 October 2019; revised manuscript received 2 May 2020; accepted 28 May 2020; published 22 June 2020)

Recently, all-inorganic two-dimensional (2D) Ruddlesden-Popper (RP) halide perovskites have drawn much attention due to their excellent stability in ambient air. However, their electronic and optical performance resulting from a wide bandgap and low carrier mobility have hindered their use in photodetectors. To overcome these limitations, in this work, taking advantage of hexagonal indium selenide (InSe) with a high electron mobility, we construct an atomically thin heterostructure. Density-functional-theory (DFT) calculations of the electronic and optical properties are performed for these heterostructures. The results demonstrate that the photodetection response spectrum of the heterostructures is significantly broadened as the bandgap decreases from 2.17 to 0.40 eV for the InSe/$Cs_2SnI_2Cl_2$ heterostructure. Moreover, the electron effective mass, m_e^*, is reduced from 1.13 m_0 to 0.41 m_0 for the InSe/$Cs_2GeI_2Cl_2$ heterostructure. The significant reductions in both the band gap and effective mass are determined to be related to the type-II band alignment, which favors the carrier separation at the interface. The physical mechanisms related to the usage of this material in photodetectors are also discussed. The proposed III–VI semiconductor InSe and all-inorganic 2D RP perovskite $Cs_2XI_2Cl_2$ ($X = $ Pb, Sn, and Ge) heterostructures provide challenges and opportunities for designing high-performance photodetectors.

DOI: 10.1103/PhysRevApplied.13.064053

I. INTRODUCTION

Metal halide perovskites have drawn much attention owing to their excellent electronic and optical properties, such as their long charge-carrier diffusion lengths, high carrier mobilities, and large absorption coefficients [1–4]. To date, significant progress has been made as the power-conversion efficiency has reached 25.2% for perovskite solar cells. [5] However, the intrinsic poor moisture and thermal stabilities of these perovskite solar cells prevent them from being widely applied [6,7].

With a decrease of the dimensionality from three dimensions (3D) to two dimensions (2D), 2D Ruddlesden-Popper (RP) halide perovskites have exhibited improved intrinsic stability [8]. These 2D RP perovskites are usually formed by inorganic octahedron layers cleaved along the ⟨100⟩-oriented layers from the ABX_3 structure, and are separated by two layers of barrier atoms [9,10]. The general formula for these 2D RP perovskites is $A_{n+1}B_nX_{3n+1}$ ($n = 1, 2, 3, \ldots$), where A is a long-chain organic cation or small inorganic atom, B is a divalent metallic element, and X is a halide anion. There are two types of 2D RP halide perovskites according to the A site element: organic-inorganic 2D RP perovskites and all-inorganic 2D RP perovskites. The organic-inorganic 2D RP perovskites show an enhanced stability relative to their 3D counterparts. For instance, Smith *et al.* [11] reported that solar-cell devices that adopted $(PEA)_2(MA)_2Pb_3I_{10}$ as absorbers exhibited enhanced moisture stability compared to $(MA)PbI_3$ thin films. Additionally, Chen *et al.* [12] fabricated $(iso\text{-}BA)_2(MA)_3Pb_4I_{13}$ using a hot-casting technique and found that $(iso\text{-}BA)_2(MA)_3Pb_4I_{13}$ essentially maintained its optical absorption levels after 840 h when exposed to a 60% relative humidity condition. Nevertheless, the intrinsic moisture sensitivity of these perovskite solar cells in ambient air remains an issue for both long-term operation and large-scale device fabrication. [11] In contrast to organic-inorganic 2D RP perovskites, all-inorganic 2D RP homologs exhibit better intrinsic stabilities but are more difficult to fabricate [13]. Recently, Li *et al.* [13,14] successively synthesized all-inorganic RP halide perovskites, $Cs_2SnI_2Cl_2$ and $Cs_2PbI_2Cl_2$, using a solid-state method, and these were shown to be stable for

---

[*] mqcai@hnu.edu.cn

up to 4 months in ambient air with 65% humidity. However, inferior photoelectric properties, including a wide bandgap (up to 3.04 eV for $Cs_2PbI_2Cl_2$) and low carrier mobility, limit the potential applications of these materials in photodetectors [13,15]. The optical properties of such all-inorganic 2D RP perovskites must therefore be improved.

Constructing a type-II van der Waals (vdW) heterostructure with a suitable semiconductor is usually an effective way to enhance the optical properties of perovskites. These types of geometric and electronic structures permit the use of the excellent properties of the two involved components [16,17]. Ma *et al.* [18] fabricated a $MAPbI_3$-WS_2 heterostructure via vapor deposition and found that the dark current was suppressed while the photocurrent was enhanced by more than 1 order of magnitude. Moreover, the on and off switching of the heterostructure was improved by 5 orders of magnitude compared to that of pure perovskites. Liu *et al.* [19] theoretically investigated $CsPbI_3$-black phosphorus (BP) monolayer heterostructures based on density-functional-theory (DFT) calculations. Their results demonstrated that the Cs-I-BP interface is a typical type-II heterostructure and the BP monolayer effectively improved the absorption coefficient of the $CsPbI_3$ perovskite.

As a III-VI semiconductor, the layered InSe with an indirect bandgap shows promise as a suitable material for constructing an InSe/all-inorganic 2D RP perovskite heterostructure owing to the tunable bandgaps, good air stability, and especially high electron mobility [20,21]. Recently, monolayer and few-layer InSe were successfully experimentally synthesized via mechanical exfoliation and demonstrated better stability than GaSe, as confirmed by microphotoluminescence (PL) and Raman spectroscopy [20,22,23]. Few-layer InSe has also been widely used in photodetectors, demonstrating a broadband response in the near-infrared and visible to ultraviolet light regions, a strong photoresponse of 34.7 mA/W, and a fast response time of 488 us, superior to that of MoS_2 and graphene [22,24,25]. Moreover, Sucharitakul *et al.* demonstrated that InSe has a high electron mobility [$>10^3$ $cm^2/(V^{-1}$ $s^{-1})$] at room temperature [26]. Despite the progress that has been made with 2D RP perovskites, improving the photoelectronic properties of all-inorganic 2D RP perovskites has not yet been explored. Considering this, it is important to investigate the interface engineering of $InSe/Cs_2XI_2Cl_2$ ($X=$ Pb, Sn, and Ge) heterostructures with enhanced optoelectronic properties for potential use in high-performance photodetectors.

In this work, we investigate the electronic and optical properties of these materials, including the band structures, carrier-transport properties, interface charge-transport mechanisms, and absorption coefficients of the $InSe/Cs_2XI_2Cl_2$ ($X=$ Pb, Sn, and Ge) vdW heterostructures using DFT calculations. Our results demonstrate that the $InSe/Cs_2XI_2Cl_2$ ($X=$ Pb, Sn, and Ge) heterostructures show an enhanced electronic and optical performance compared with the all-inorganic 2D RP perovskites, indicating that they are promising candidates for photodetector applications.

II. METHODS

Our DFT calculations are performed using the Vienna *ab initio* simulation package (VASP) [27]. The exchange correlation functional is parametrized by the Perdew, Burke, and Ernzerhof (PBE) model [28]. The Heyd-Scuseria-Ernzerhof (HSE06) hybrid functional [29] is used to calculate accurate bandgap values. Spin-orbit coupling (SOC) [30] is also included. The choice of $\alpha=43\%$ for the HSE mixing parameter is based on Ref. [31]. For structural relaxations, the DFT-D3 method [32] is chosen to account for the vdW interactions. For the structural relaxation, a cutoff energy of 400 eV is used. A $5\times5\times1$ Monkhorst-Pack K-mesh is used to sample the two-dimensional Brillouin zone. The energy convergence threshold is 1.0×10^{-5} eV and the criteria for the convergence of the Hellmann-Feynman forces on the atoms is 0.02 eV/Å. The crystal structures are visualized using VESTA [33].

The effective mass, m^*, associated with the band dispersion is derived using $m^*=\hbar^2[\partial^2\varepsilon(k)/\partial k^2]^{-1}$, where k is a wave vector and $\varepsilon(k)$ represents the energy eigenvalues. The k-projection method, as implemented in the program KPROJ [34,35], is also used to obtain unfold bands for the heterostructures as supercells are involved in this type of interface structure. The absorption coefficient is calculated based on the formula $\alpha=(\sqrt{2})\omega\left[\sqrt{\varepsilon_1(\omega)^2+\varepsilon_2(\omega)^2}-\varepsilon_1(\omega)\right]^{1/2}$ [36]. The dielectric functions are calculated by $\varepsilon(\omega)=\varepsilon_1(\omega)+i\varepsilon_2(\omega)$ [37], where $\varepsilon_1(\omega)$ and $\varepsilon_2(\omega)$ present the real part and the imaginary part, and ω is the photon frequency. The imaginary part could be acquired as follows [38]: $\varepsilon_2(\hbar\omega)=4\pi^2e^2/\phi\varepsilon_0\sum_{c,v,k}|\varphi_k^c|u\cdot r|\varphi_k^v|^2\delta(E_k^c-E_k^v-E)$, where ε_0 and φ present vacuum dielectric constant and crystal volume, respectively. The E_k^c and E_k^v are the energy of CB and VB, u represents the vector of polarization for the incident electric field, and $\mu\cdot r$ is the momentum operator. The real part $\varepsilon_1(\omega)$ can be expressed from the Kramers-Kronig relationship as follows: $\varepsilon_1(\omega)=1+\frac{2}{\pi}P\int_0^\infty[\varepsilon_2(\omega')\omega']/(\omega'^2-\omega^2+i\eta)d\omega'$, where P and η are the principle value of integrals and the refractive index, respectively.

III. RESULTS AND DISCUSSION

A. Geometric structures

To investigate the $InSe/Cs_2XI_2Cl_2$ ($X=$ Pb, Sn, and Ge) heterostructures, we first discuss the free-standing

InSe monolayer and the $Cs_2XI_2Cl_2$ ($X = $ Pb, Sn, and Ge) monolayer. Figure 1(a) shows the bulk phase of InSe with a hexagonal structure, while the top and side views of the InSe monolayer are shown in Figs. 1(c) and 1(d), respectively. The optimized lattice constants for the InSe monolayer are $a = b = 4.08$ Å, which agree with the previous experimental and calculational results. [39,40] The bulk all-inorganic 2D RP perovskites $Cs_2XI_2Cl_2$ ($X = $ Pb, Sn, and Ge) are shown in Fig. 1(b). The bulk $Cs_2XI_2Cl_2$ ($X = $ Pb, Sn, and Ge) adopt the K_2NiF_4-type structure and the tetragonal space group with $I4/mmm$ symmetry. Figures 1(e) and 1(f) show the top and side views of the $Cs_2XI_2Cl_2$ monolayer ($X = $ Pb, Sn, and Ge), respectively. The atomic structures for $Cs_2XI_2Cl_2$ ($X = $ Pb and Sn) are directly determined using experimental results [13,14], wherein the lattice constants for $Cs_2PbI_2Cl_2$ are $a = b$=5.64 Å and those for $Cs_2SnI_2Cl_2$ are $a = b = 5.59$ Å. Additionally, the atomic configuration for $Cs_2GeI_2Cl_2$ is fully optimized by substituting Pb with Ge atoms in the $Cs_2PbI_2Cl_2$ structure, and the lattice constants are $a = b = 5.46$ Å. The constructed InSe/$Cs_2XI_2Cl_2$ ($X = $ Pb, Sn, and Ge) heterostructures using the QuantumATK package [41] are illustrated in Fig. 1(g). The unit cell of the heterostructure is composed of a $\sqrt{2} \times \sqrt{2}$ perovskite monolayer supercell and a $2 \times \sqrt{3}$ InSe monolayer supercell as shown in Fig. S1 within the Supplemental Material [42]. The mean lattice mismatch values for the InSe/$Cs_2PbI_2Cl_2$, InSe/$Cs_2SnI_2Cl_2$, and InSe/$Cs_2GeI_2Cl_2$ heterostructures are 2.39%, 2.40%, and 2.40%, respectively, which are in a reasonable range [43,44]. The distance of the vacuum space is set to 15 Å to avoid the interaction of adjacent slabs. The vertical heterostructures can be combined in three different stacking types (AA, AB, and AC) as shown in Fig. 2. The total energy calculations reveal that AB for the InSe/$Cs_2PbI_2Cl_2$ heterostructure is the ground-state stacking type with the vertical interlayer distance (3.16 Å). The total energy differences are found to vary from 9.8 to 27.3 meV per unit cell. Besides, as shown in Table S1 within the Supplemental Material [42], the AB type is also the ground-state stacking type for the InSe/$Cs_2SnI_2Cl_2$

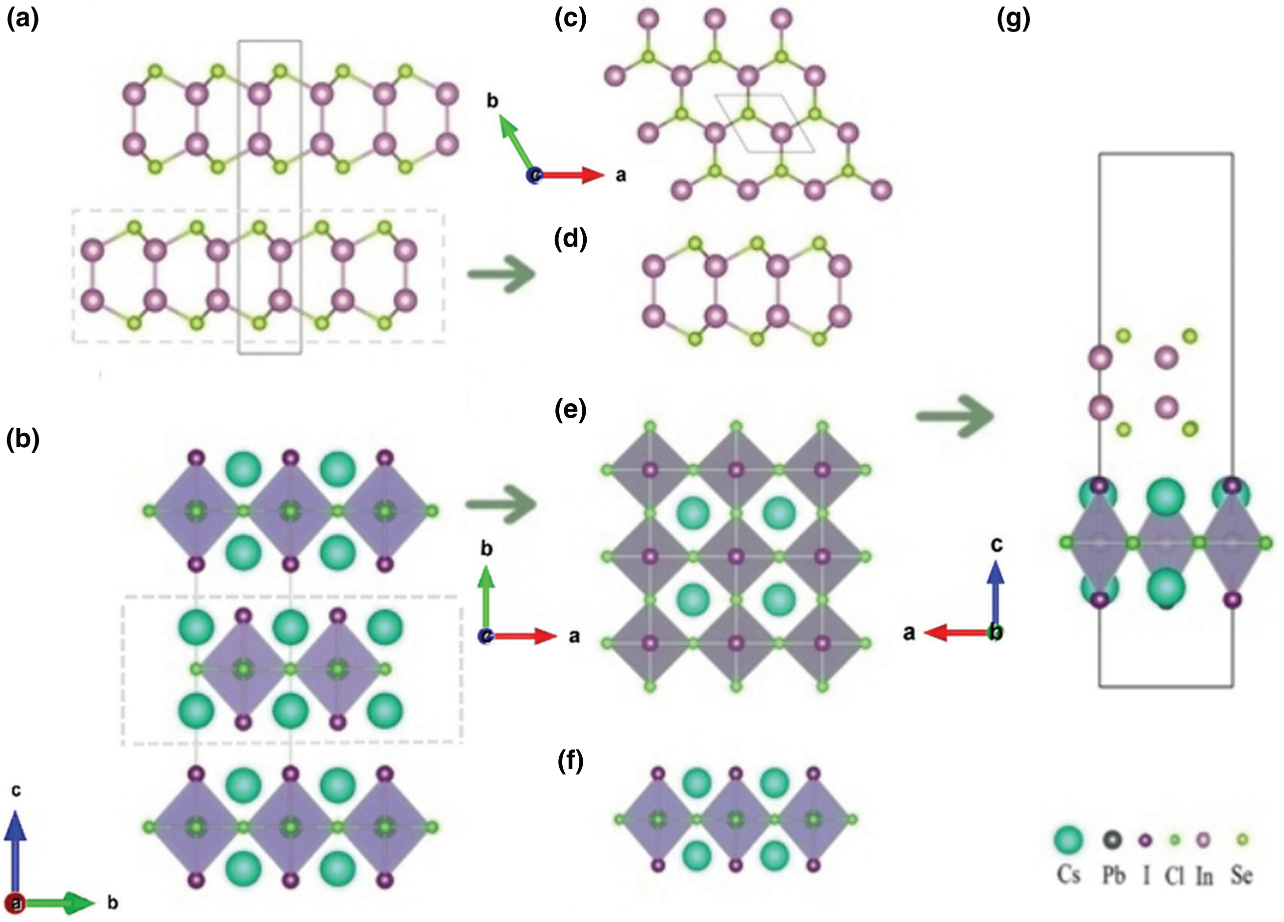

FIG. 1. Structures of InSe/$Cs_2XI_2Cl_2$. (a), (b) Structures of the bulk phases of InSe and $Cs_2PbI_2Cl_2$, respectively. (c) Top view and (d) side view of the InSe monolayer. (e), (f) Structures of the $Cs_2PbI_2Cl_2$ monolayer. (g) Geometric structure of the InSe/$Cs_2PbI_2Cl_2$ heterostructure. The dotted boxes and olive-colored arrows demonstrate the formation of the heterostructure. The atomic color code is as follows: green, Cs; gray, Pb; purple, I; light green, Cl; pink, In; yellow, Se.

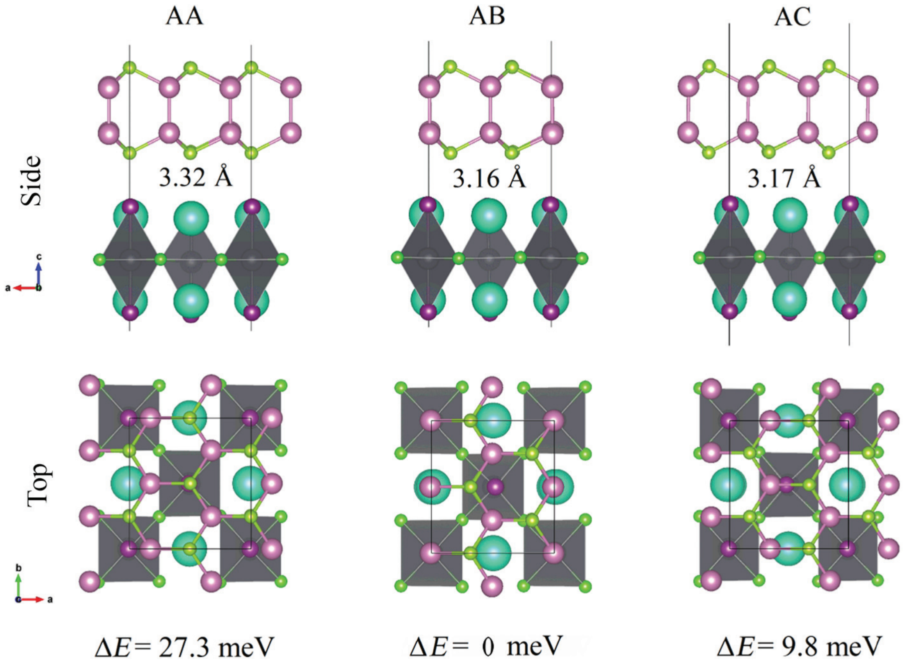

FIG. 2. Top and side views of various stacking configurations for InSe/$Cs_2PbI_2Cl_2$ heterostructures. The total energy differences with respect to the ground-state stacking and the vertical-interlayer distances are also given.

heterostructure and InSe/$Cs_2GeI_2Cl_2$ with the interlayer distance 3.27 and 3.20 Å. Therefore, we choose the AB stacking configuration as our study object. Additionally, the interface formation energies are calculated according to the formula $\Delta E = (E_{\text{hete}} - E_{\text{PVK.}} - E_{\text{InSe}})/S$, [45], where E_{hete}, E_{PVK}, and E_{InSe} represent the total energies of the heterostructure, perovskites, and InSe in the heterostructure lattice, respectively, and S is the area of the interface. The interface formation energies for the InSe/$Cs_2PbI_2Cl_2$, InSe/$Cs_2SnI_2Cl_2$, and InSe/$Cs_2GeI_2Cl_2$ heterostructures are -1.29, -1.02, and -1.35 meV/Å^2, respectively, more stable than the TiO_2/SnO_2-(110) heterostructure [45]. Both of the interface formation energies are negative, demonstrating these heterostructures are stable and the InSe/$Cs_2GeI_2Cl_2$ heterostructure forms more easily. The lattice constants of these heterostructures are provided in Table S2 within the Supplemental Material [42].

B. Electronic band structures and carrier-transport properties

The band structures and projected density of states (PDOS) for the primitive cells of the InSe monolayer and $Cs_2PbI_2Cl_2$ monolayer are calculated with PBE functionals, as shown in Fig. 3. In Fig. 3(a), the conduction-band minimum (CBM) of the InSe monolayer is located at point Γ while the VBM is located between points M and Γ in the Brillouin zone. The InSe monolayer therefore has an indirect bandgap of 1.39 eV, which is in agreement with the previously calculated value of 1.323 eV [46]. As shown in Fig. 3(b), the PDOS of the InSe monolayer shows that the CBM consists of In (s) and Se (p) orbitals, and the VBM is largely composed of the p orbitals of Se and s orbitals of In atoms. Besides, the VBM of primitive InSe monolayer attains a Mexican-hat-type dispersion near the Γ point, which leads to a van Hove singularity in the DOS near the Fermi level [47–51]. This van Hove singularity can affect the thermoelectric performance and leads to a ferromagnetic phase transition at sufficient hole doping [52,53]. In Fig. 3(c), $Cs_2PbI_2Cl_2$ monolayer is shown to have a direct bandgap energy of 2.46 eV, with the CBM and VBM both located at point M in the Brillouin zone. The value of the bandgap calculated with PBE functionals for $Cs_2PbI_2Cl_2$ is underestimated by about 0.6 eV compared with the value 3.04 eV [13], which is discussed in the following paragraph. Furthermore, as seen in Fig. 3(d), only the Pb (p) orbital contributes to the CBM, while the VBM mainly consists of the I (p) orbital, with small contributions from the Pb (s) and Cl (p) orbitals. The band structures and PDOS of the $Cs_2GeI_2Cl_2$ and $Cs_2SnI_2Cl_2$ monolayer are presented in Fig. S2 within the Supplemental Material [42]. The bandgaps calculated with PBE functionals for $Cs_2SnI_2Cl_2$ and $Cs_2GeI_2Cl_2$ are 1.54 and 1.73 eV, respectively.

The electronic band structures of the heterostructures are determined and the bandgaps using several different functionals are presented in Table I. The bandgaps for the InSe/$Cs_2PbI_2Cl_2$ and InSe/$Cs_2GeI_2Cl_2$ heterostructures calculated with PBE functionals are 0.42 and 0.55 eV, respectively, while a type-III heterostructure is present at the InSe/$Cs_2SnI_2Cl_2$ interface as shown in Fig. S3 within the Supplemental Material [42]. In addition, the bandgap for the single-layer perovskite in heterostructure lattice (2.20, 1.26, and 1.55 eV for $Cs_2PbI_2Cl_2$, $Cs_2SnI_2Cl_2$, and $Cs_2GeI_2Cl_2$, respectively) calculated with the PBE

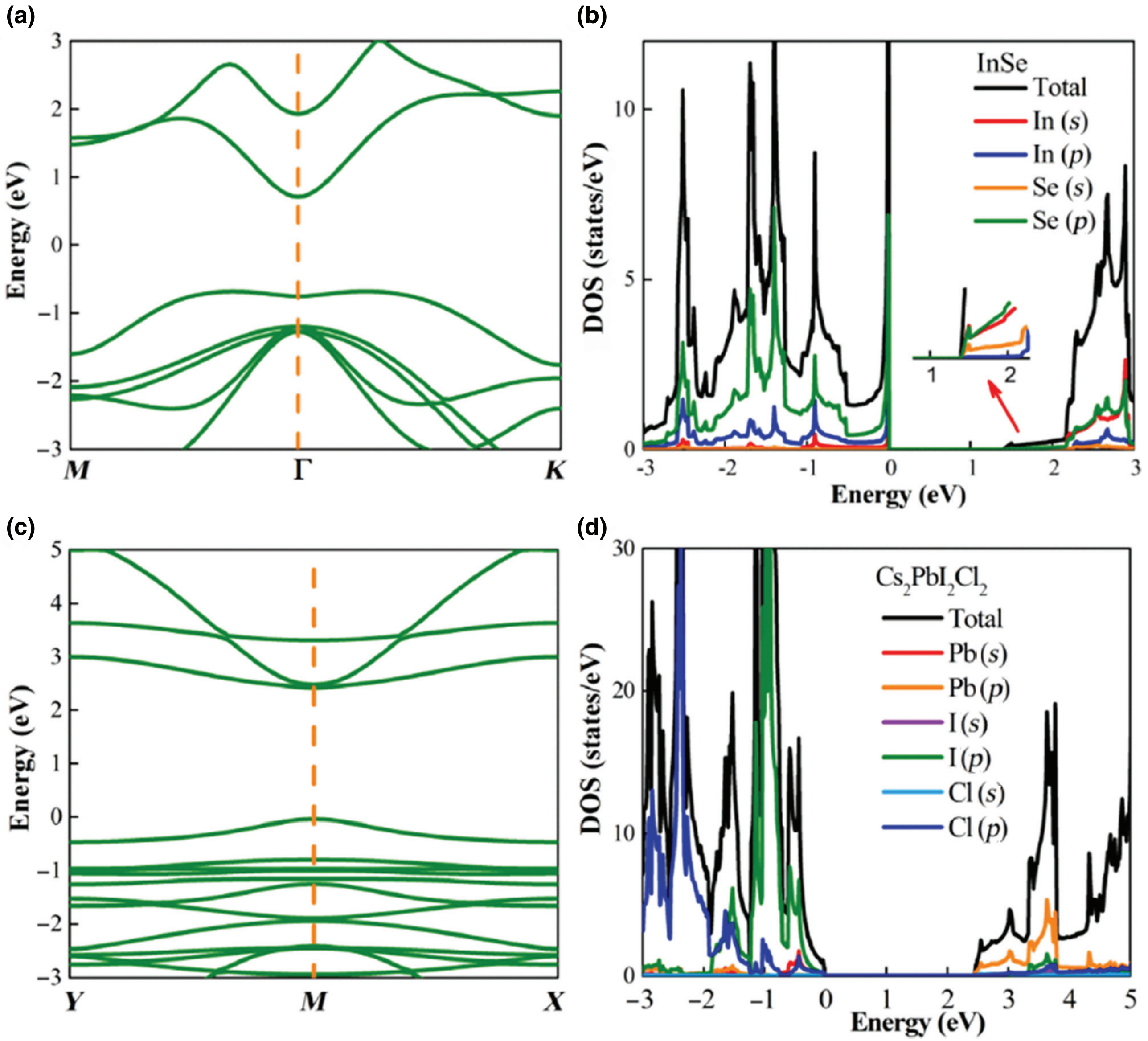

FIG. 3. (a) Band structure and (b) PDOS of the InSe monolayer. (c) Band structure and (d) PDOS of the $Cs_2PbI_2Cl_2$ monolayer using PBE functional. The red arrow indicates the magnified area at about 1.5 eV.

functional is similar to that of the primitive single layer (2.46, 1.54, and 1.73 eV for $Cs_2PbI_2Cl_2$, $Cs_2SnI_2Cl_2$, and $Cs_2GeI_2Cl_2$, respectively), indicating the small influence of the lattice mismatch on the bandgaps. This trend is also observed for the InSe monolayer. The PBE included SOC effect is adopted to calculate the band structures. As seen in Fig. S4 (within the Supplemental Material [42]), there is no Rashba-type spin splitting of the CBM and VBM of heterostructures near the Γpoint [54–59]. The SOC effect only reduces the bandgaps. The bandgaps of $Cs_2SnI_2Cl_2$ and $Cs_2GeI_2Cl_2$ monolayers reduced from 1.26 and 1.55 eV to 1.14 and 1.46 eV, while the bandgap of $Cs_2PbI_2Cl_2$ decreased by 0.7 eV. The results reveal that the SOC effect has a great influence on bandgap for Pb-based systems, but little influence on that for Sn- and Ge-containing systems. However, the bandgaps for the free-standing $Cs_2PbI_2Cl_2$ (2.20 eV) and $Cs_2SnI_2Cl_2$ (1.26 eV) calculated by PBE functional are much less than those previously reported for $Cs_2PbI_2Cl_2$ (3.04 eV) and $Cs_2SnI_2Cl_2$ (2.6 eV) [13,14]. Therefore, to improve the calculational accuracy of the band structures, the bandgaps are calculated with the HSE06+SOC functional. The calculated bandgaps using the HSE06+SOC functional for the InSe monolayer (2.22, 2.29, or 2.52 eV) in heterostructure lattice are closed to the other experimental (2.4–2.6 eV) [20] and theoretical results (2.16 eV) [60]. Besides, the calculated bandgaps using the HSE06+SOC functional for the $Cs_2PbI_2Cl_2$ monolayer (2.75 eV) in the

TABLE I. Calculated bandgaps (eV) for free-standing InSe, $Cs_2XI_2Cl_2$ (X = Pb, Sn, and Ge) and heterostructures with PBE, PBE+SOC, HSE06, and HSE06+SOC functionals, respectively.

	X	InSe	$Cs_2XI_2Cl_2$	Heterostructures
HSE06+SOC	Pb	2.22	2.75	1.37
	Sn	2.29	2.17	0.40
	Ge	2.52	2.67	1.55
HSE06	Pb	2.25	3.40	1.44
	Sn	2.33	2.25	0.42
	Ge	2.55	2.71	1.59
PBE+SOC	Pb	0.91	1.52	0.41
	Sn	0.97	1.14	III
	Ge	1.15	1.46	0.56
PBE	Pb	0.93	2.20	0.42
	Sn	0.99	1.26	III
	Ge	1.18	1.55	0.55

heterostructure lattice are closed to the other experimental (3.04 eV) [13] and theoretical results (2.99 eV) [31], while the bandgaps for the $Cs_2SnI_2Cl_2$ monolayer (2.17 eV) are a little smaller than experimental (2.62 eV) and theoretical results (2.51 eV) [14,31]. The band structures for the InSe/$Cs_2PbI_2Cl_2$, InSe/$Cs_2SnI_2Cl_2$, and InSe/$Cs_2GeI_2Cl_2$ heterostructures calculated with the HSE06+SOC functional are shown in Figs. 4(a)–4(c). The results show that these three heterostructures are all direct type-II band alignment at point Γ. Only the InSe monolayer contributes to the CBM, while the VBM consists of the all-inorganic 2D RP perovskites. The bandgaps for the InSe/$Cs_2PbI_2Cl_2$ and InSe/$Cs_2GeI_2Cl_2$ heterostructures calculated using the HSE06+SOC functional are 1.37 and 1.55 eV, respectively, while the bandgap for the InSe/$Cs_2SnI_2Cl_2$ heterostructure is relatively small (0.40 eV). The smaller bandgap (0.40 eV) for the InSe/$Cs_2SnI_2Cl_2$ heterostructure demonstrates it can detect the wider photodetection response spectrum. Notably, the bandgap of these heterostructures using the HSE06 functional as shown in Fig. S5 (within the Supplemental Material [42]) are similar to that calculated using the HSE06+SOC functional.

To investigate the carrier-transport properties of the heterostructures, the effective mass, m^*, in the a-b plane of the CBM and VBM at the bandgap is calculated. From the band structures we extract the effective masses of electrons and holes around the CBM and VBM according to the formula: $m^* = \hbar^2[\partial^2\varepsilon(k)/\partial k^2]^{-1}$. The effective electron and hole masses of the InSe monolayer, $Cs_2XI_2Cl_2$ monolayer (X = Pb, Sn, and Ge), and InSe/$Cs_2XI_2Cl_2$ heterostructures using several different functionals are listed in Table S3 within the Supplemental Material [42]. We note that effective masses using the HSE06 functional is similar to those at the PBE level, which is attributed to the fact that the HSE06 functional has little influence on dispersity of band structure. However, the SOC effect has a great influence on the dispersity of the band structure for Pb-based systems, but little influence on that for Ge- and Sn-containing systems. The effective mass of electron in InSe determined with the PBE+SOC functional is 0.48 m_0 while effective mass of the hole is 1.98 m_0, which is consistent with the high electron mobility of InSe in Refs. [20,21]. The results demonstrate that the effective masses of carriers for the heterostructures are reduced compared with those of primitive InSe, $Cs_2XI_2Cl_2$ (Pb, Se, and Ge) monolayers, among which, the electron effective mass is reduced from 1.13 m_0 to 0.41 m_0 for the InSe/$Cs_2GeI_2Cl_2$ heterostructure.

To clarify the physical mechanism, we study the contributions of different constituents in heterostructure systems.

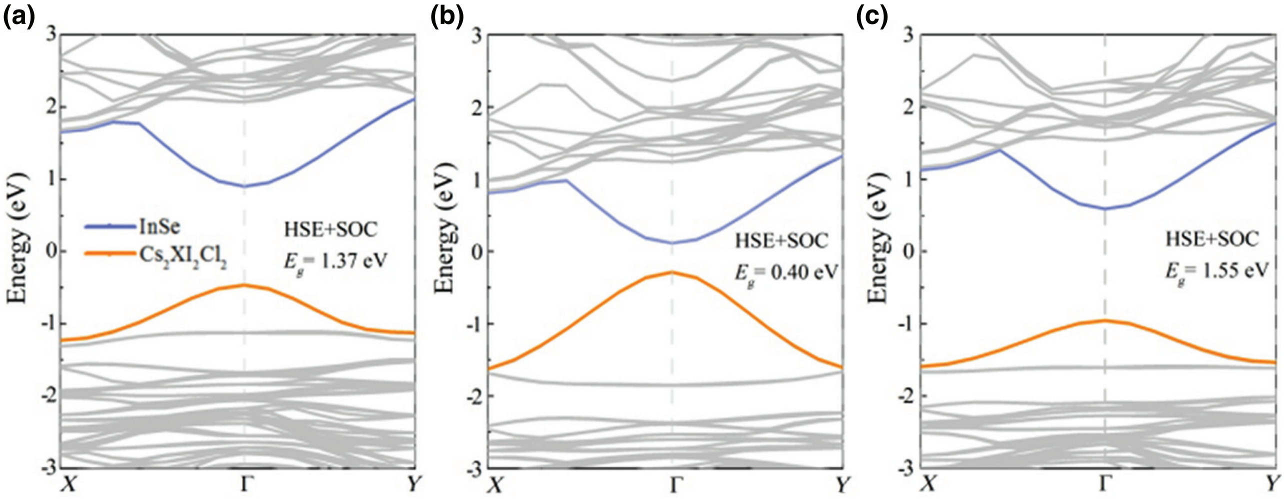

FIG. 4. Electronic bands determined from HSE06+SOC calculation for the (a) InSe/$Cs_2PbI_2Cl_2$, (b) InSe/$Cs_2SnI_2Cl_2$, and (c) InSe/$Cs_2GeI_2Cl_2$ heterostructures. The blue and yellow lines denote the contributions from InSe and the 2D RP perovskite, respectively.

Owing to the supercells we adopt in our systems, the folding bands appear and influence the direct comparison with intrinsic electronic band structure of the 1 × 1 cell. Therefore, to reveal the real electronic band structures of the interface, the *k*-projection technique [34,35] is used to unfold the band structures from the supercell calculations and provide a local band structure, which is efficiently performed by adopting fast Fourier transforms. Figures 5(a) and 5(c) are the band structures of free-standing InSe and $Cs_2PbI_2Cl_2$ in heterostructure lattice. These band structures could not simply resemble those of primitive $Cs_2PbI_2Cl_2$ and InSe monolayers as shown in Figs. 3(a) and 3(c). After doing the *k* projection to the 1 × 1 cell as shown in Figs. 5(b) and 5(d), the unfolded bands closely resemble the primitive monolayers. The results demonstrate that the bandgap of the heterostructure is the result of hybridization between the $Cs_2PbI_2Cl_2$ and InSe monolayer. It should be noted that because of the strain resulting from the lattice mismatch, the X and Y points in the Brillouin zone of the supercells have a slight displacement, which has little impact on the location of these folded bands.

C. Interface charge-transport mechanism

To explore the charge-transfer mechanism at the InSe/$Cs_2XI_2Cl_2$ ($X = $Pb, Sn, and Ge) interface, we calculate the differential charge density according to the formula $\Delta\rho(z) = \rho_{\text{hete}} - \rho_{Cs_2XI_2Cl_2} - \rho_{\text{InSe}}$ [19]. The planar-averaged differential charge densities for the InSe/$Cs_2XI_2Cl_2$ ($X = $Pb, Sn and Ge) heterostructures along the z direction are presented in Figs. 6(d)–6(f). The

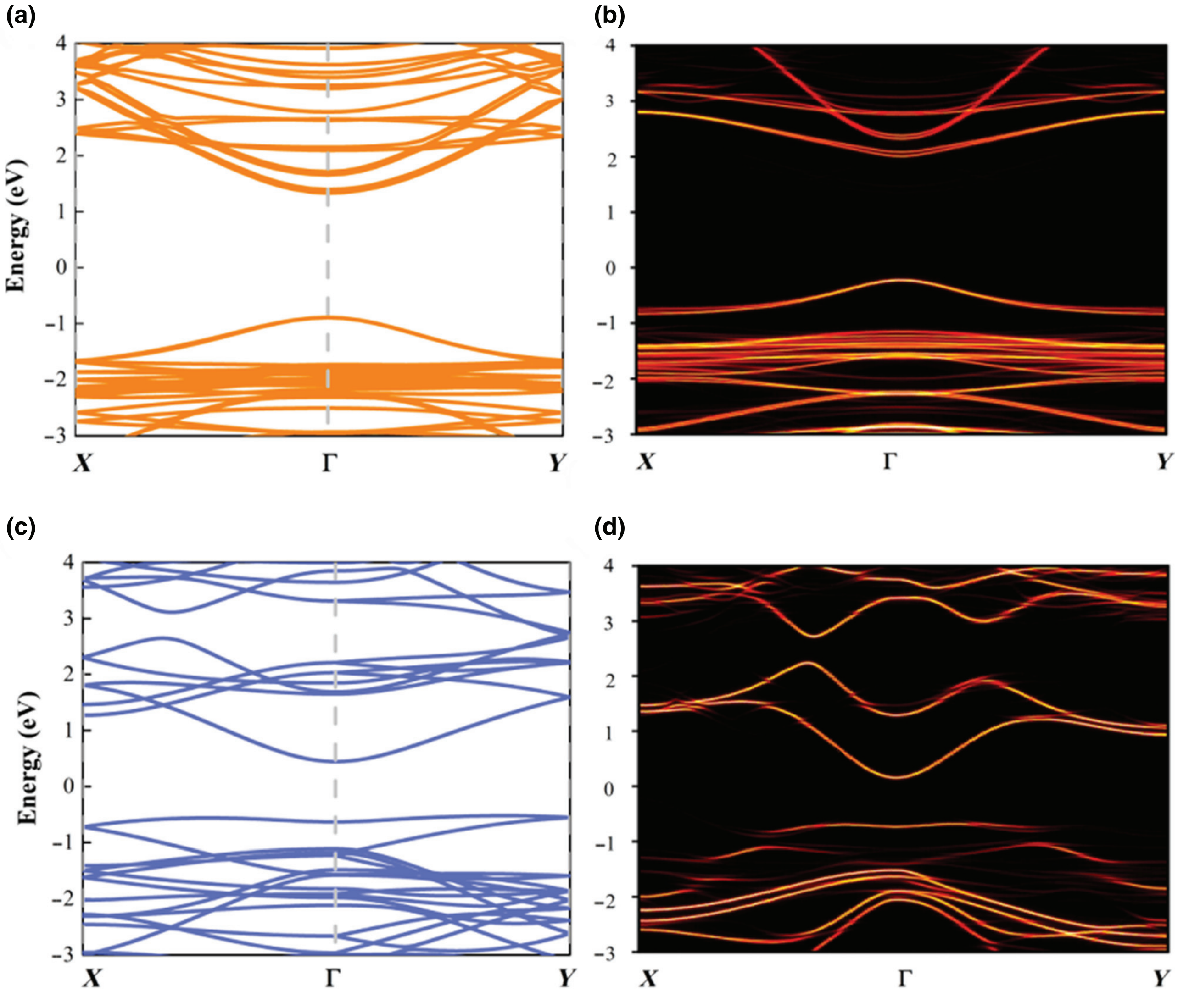

FIG. 5. Band structures for the free-standing $Cs_2PbI_2Cl_2$ and InSe in the heterostructure lattice using the PBE functional are respectively shown in (a) and (c). The unfolded bands derived from the *k*-projection method are shown in (b),(d). The Fermi level is set to be zero.

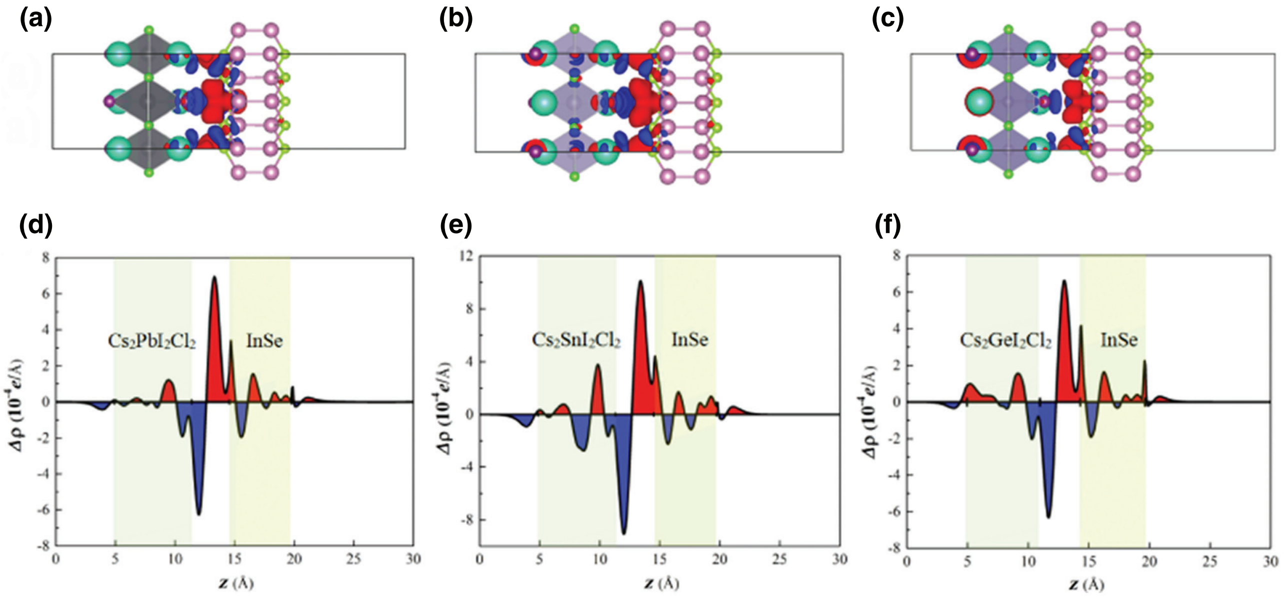

FIG. 6. Differential charge densities using the PBE functional for the (a) InSe/$Cs_2PbI_2Cl_2$, (b) InSe/$Cs_2SnI_2Cl_2$, and (c) InSe/$Cs_2GeI_2Cl_2$ heterostructures, respectively. (d)–(f) Planar-averaged differential charge densities $\Delta\rho(z)$ for the structural models shown in (a)–(c), respectively. The red and blue colors indicate electron accumulation and depletion, respectively.

red charge area indicates charge accumulation, while the blue charge area indicates charge depletion. It can be seen that the charge at the interface flows from the all-inorganic 2D RP perovskite to the InSe monolayer, which restricts the recombination of electrons and holes. The differential charge densities for the InSe/$Cs_2XI_2Cl_2$ ($X = $ Pb, Sn, and Ge) interfaces are also provided in Figs. 6(a)–6(c). The accumulated charge cloud is shown to be concentrated around the Se atoms, while the depleted charge cloud is concentrated around the I atoms. Moreover, the work function is calculated to demonstrate the charge movement. The values of the work functions for the heterostructures, free-standing InSe, and all-inorganic 2D RP perovskite are listed in Table S4 within the Supplemental Material [42]. Considering the Pb-based heterostructures, the value of the work function for free-standing InSe, 5.33 eV, is larger than that of $Cs_2PbI_2Cl_2$, 4.55 eV. The charge would therefore move from $Cs_2PbI_2Cl_2$ to InSe until they possess the same work-function values. When InSe and $Cs_2PbI_2Cl_2$ are in contact, the work function for the heterostructure is 4.95 eV, which is a moderate value compared with those of InSe (5.33 eV) and $Cs_2PbI_2Cl_2$ (4.59 eV).

D. Optical properties

To explore the influence of the InSe monolayer on the absorption coefficient of the heterostructures, we calculate the absorption coefficients of the heterostructures, InSe monolayer, and all-inorganic 2D RP perovskites using PBE functionals according to the formula $\alpha = (\sqrt{2})\omega\left[\sqrt{\varepsilon_1(\omega)^2+\varepsilon_2(\omega)^2}-\varepsilon_1(\omega)\right]^{1/2}$. It is worth noting that the PBE functional are adopted rather than the

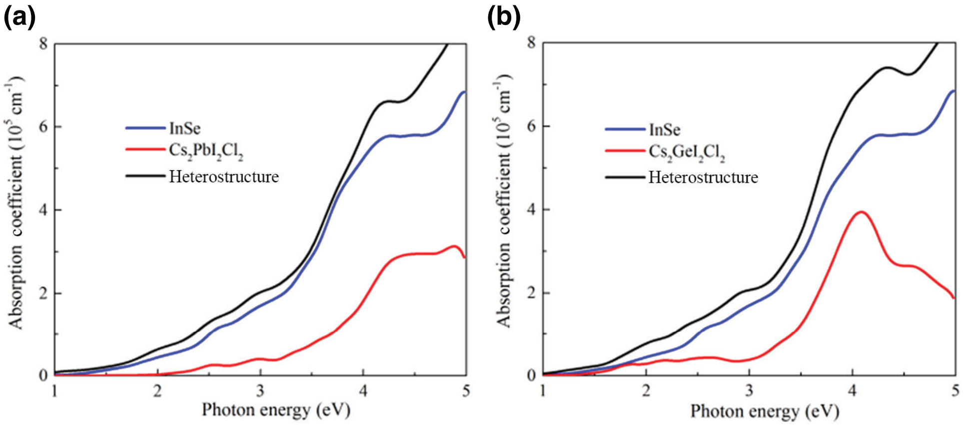

FIG. 7. Calculated absorption coefficients for the (a) InSe/$Cs_2PbI_2Cl_2$ and (b) InSe/$Cs_2GeI_2Cl_2$ heterostructures using the PBE functional. The blue, red, and black lines represent the InSe, 2D RP perovskite, and heterostructure, respectively.

HSE06+SOC functional to calculate the absorption coefficient as computational resources are limited [61–74]. Considering the type-III heterostructure that is identified at the InSe/$Cs_2SnI_2Cl_2$ interface via the PBE functional, we calculate the absorption coefficients of the InSe/$Cs_2PbI_2Cl_2$ and InSe/$Cs_2GeI_2Cl_2$ heterostructures for comparison between the heterostructures, free-standing InSe, and perovskites. This allowed for the qualitative analysis of the influence of the InSe monolayer on the absorption coefficient of the heterostructure. The calculated absorption coefficients of the InSe/$Cs_2PbI_2Cl_2$ and InSe/$Cs_2GeI_2Cl_2$ heterostructures are shown in Figs. 7(a) and 7(b). It can be seen that the all-inorganic 2D RP perovskites $Cs_2PbI_2Cl_2$ and $Cs_2GeI_2Cl_2$ show small absorption coefficients in the visible region compared with that of the InSe monolayer. The absorption coefficient of the InSe/$Cs_2XI_2Cl_2$ ($X = $Pb and Ge) heterostructures are also shown to be greatly enhanced. Owing to the bandgap reduction from 2.17 to 0.40 eV for the InSe/$Cs_2SnI_2Cl_2$ heterostructure, the absorption spectrum of the heterostructures are broadened to incorporate the near-infrared region, which is more favorable for application in high-performance photodetectors, compared with Pb- and Ge-based heterostructures.

IV. CONCLUSION

In summary, the electronic and optical properties of the InSe/$Cs_2XI_2Cl_2$ ($X = $Pb, Sn, and Ge) vdW heterostructures are investigated via DFT calculations. Our results demonstrate that the photodetection response spectrum of the InSe/$Cs_2SnI_2Cl_2$ heterostructure is dramatically broadened as the bandgap decreased from 2.17 to 0.40 eV, and an enhanced absorption coefficient is observed compared to the isolated systems. Moreover, the electron effective mass is reduced from 1.13 m_0 to 0.41 m_0 for the InSe/$Cs_2GeI_2Cl_2$ heterostructure. These enhancements are ascribed to the type-II energy-band alignment, wherein the InSe monolayer contributes to the CBM while the VBM results from the all-inorganic 2D RP perovskites. Band unfolding further supports such a band alignment for this type of heterostructure, which favors carrier separation. Our results indicate that the InSe/$Cs_2XI_2Cl_2$ ($X = $Pb, Sn, and Ge) vdW heterostructures are promising candidates for use in high-performance photodetectors.

ACKNOWLEDGMENTS

The authors thank the Changsha Supercomputer Center for computation. This work is supported by the National Natural Science Foundation of China (Grants No. 51972103 and No. 21938002), the Key Projects of Hunan Provincial Science and Technology Plan (Grant No. 2017GK2231), and the Hunan Provincial Innovation Foundation for Postgraduate (Grant No. CX2018B161).

[1] S. D. Wolf, J. Holovsky, S. J. Moon, P. Löper, B. Niesen, M. Ledinsky, F. J. Haug, J. H. Yum, and C. Balli, Organometallic halide perovskites:Sharp optical absorption edge and its relation to photovoltaic performance, J. Phys. Chem. Lett. **5**, 1035 (2014).

[2] M. B. Johnston and L. M. Herz, Hybrid perovskites for photovoltaics: Charge-carrier recombination, diffusion, and radiative efficiencies, Acc. Chem. Res. **49**, 146 (2016).

[3] G. Xing, N. Mathews, S. Sun, S. S. Lim, Y. M. Lam, M. Grätzel, S. Mhaisalkar, and T. C. Sum, Long-Range balanced electronand hole-transport lengths in organic-inorganic $CH_3NH_3PbI_3$, Science **342**, 344 (2013).

[4] S. D. Stranks, G. E. Eperon, G. Grancini, C. Menelaou, M. J. P. Alcocer, T. Leijtens, L. M. Herz, A. Petrozza, and H. J. Snaith, Electron-hole diffusion lengths exceeding 1 micrometer in an organometal trihalide perovskite absorber, Science **342**, 341 (2013).

[5] Best Research-Cell Efficiency Chart, https://www.nrel.gov/pv/cell-efficiency.html (2019).

[6] A. M. Ganose, C. N. Savory, and D. O. Scanlon, Beyond methylammonium lead iodide: Prospects for the emergent field of ns^2 containing solar absorbers, Chem. Commun. **53**, 20 (2017).

[7] J. Xiong, B. Yang, C. Cao, R. Wu, Y. Huang, J. Sun, J. Zhang, C. Liu, S. Tao, Y. Gao, and J. Yang, Interface degradation of perovskite solar cells and its modification using an annealing-free TiO_2 NPs layer, Org. Electron. **30**, 30 (2016).

[8] H. Tsai, W. Nie, J. C. Blancon, C. C. Stoumpos, R. Asadpour, B. Harutyunyan, R. Verduzco, J. Crochet, S. Tretiak, L. Pedesseau, J. Even, M. A. Alam, G. Gupta, J. Lou, P. M. Ajayan, M. J. Bedzyk, M. G. Kanatzidis, and A. D. Mohite, High-efficiency two-dimensional Ruddlesden-Popper perovskite solar cells, Nature **536**, 312 (2016).

[9] Y. F. Ding, Q. Q. Zhao, Z. L. Yu, Y. Q. Zhao, B. Liu, P. B. He, H. Zhou, K. Li, S. F. Yin, and M. Q. Cai, Strong thickness-dependent quantum confinement in all-inorganic perovskite Cs_2PbI_4 with a Ruddlesden-Popper structure, J. Mater. Chem. C **7**, 7433 (2019).

[10] Z. Chen, Y. Guo, E. Wertz, and Jian Shi, Merits and challenges of Ruddlesden–Popper soft halide perovskites in electro-optics and optoelectronics, Adv. Mater. **31**, 1803514 (2018).

[11] I. C. Smith, E. T. Hoke, D. Solis-Ibarra, M. D. McGehee, and H. I. Karunadasa, A layered hybrid perovskite solar-cell absorber with enhanced moisture stability, Angew. Chem. Int. Ed. **53**, 1232 (2014).

[12] Y. Chen, Y. Sun, J. Peng, W. Zhang, X. Su, K. Zheng, T. Pullerits, and Z. Liang, Tailoring organic cation of 2D Air-stable organometal halide perovskites for highly efficient planar solar cells, Adv. Energy Mater. **7**, 1700162 (2017).

[13] J. Li, Qin Yu, Y. He, C. C. Stoumpos, G. Niu, G. G. Trimarchi, H. Guo, G. Dong, D. Wang, L. Wang, and M. G. Kanatzidis, $Cs_2PbI_2Cl_2$, All-inorganic Two-dimensional Ruddlesden-Popper mixed halide perovskite with optoelectronic response, J. Am. Chem. Soc. **140**, 11085 (2018).

[14] J. Li, C. C. Stoumpos, G. G. Trimarchi, In Chung, L. Mao, M. Chen, M. R. Wasielewski, L. Wang, and M. G. Kanatzidis, Air-Stable direct bandgap perovskite semiconductors:All-inorganic Tin-based heteroleptic halides $A_xSnCl_yI_z$ (A=Cs, Rb), Chem. Mater. **30**, 4847 (2018).

[15] M. Yu, C. Yi, N. Wang, L. Zhang, R. Zou, Y. Tong, H. Chen, Y. Cao, Y. He, Y. Wang, M. Xu, Y. Liu, Y. Jin, W. Huang, and J. Wang, Control of barrier width in perovskite multiple quantum wells for high performance green light-emitting diodes, Adv. Opt. Mater. **7**, 1801575 (2018).

[16] B. W. H. Baugher, H. O. H. Churchill, Y. Yang, and P. Jarillo-Herrero, Optoelectronic devices based on electrically tunable p-n diodes in a monolayer dichalcogenide, Nat. Nanotechnol. **9**, 262 (2014).

[17] B. Liu, M. Long, M. Q. Cai, and J. Yang, Two-dimensional van der Waals heterostructures constructed via perovskite $(C_4H_9NH_3)_2XBr_4$ and black phosphorus, J. Phys. Chem. Lett. **9**, 4822 (2018).

[18] C. Ma, Y. M. Shi, W. J. Hu, M. H. Chiu, Z. X. Liu, A. Bera, F. Li, H. Wang, L. J. Li, and T. Wu, Heterostructured $WS_2/CH_3NH_3PbI_3$ photoconductors with suppressed dark current and enhanced photodetectivity, Adv. Mater. **28**, 3683 (2016).

[19] B. Liu, M. Q. Long, M. Q. Cai, and J. L. Yang, Interface engineering of $CsPbI_3$-black phosphorus van der Waals heterostructure, Appl. Phys. Lett. **112**, 043901 (2018).

[20] D. A. Bandurin, A. V. Tyurnina, G. L. Yu, A. Mishchenko, V. Zólyomi, S. V. Morozov, R. K. Kumar, R. V. Gorbachev, Z. R. Kudrynskyi, S. Pezzini, Z. D. Kovalyuk, U. Zeitler, K. S. Novoselov, A. Patanè6, L. Eaves, I. V. Grigorieva, V. I. Fal'ko, A. K. Geim, and Y. Cao, High electron mobility, quantum Hall effect and anomalous optical response in atomically thin InSe, Nat. Nanotechnol. **12**, 223 (2017).

[21] M. Wu, J. J. Shi, M. Zhang, Y. M. Ding, H. Wang, Y. L. Cena, and J. Lu, Enhancement of photoluminescence and hole mobility in 1- to 5-layer InSe due to the top valence-band inversion: Strain effect, Nanoscale **10**, 11441 (2018).

[22] S. Lei, L. Ge, S. Najmaei, A. George, R. Kappera, J. Lou, M. Chhowalla, H. Yamaguchi, G. Gupta, R. Vajtai, A. D. Mohite, and P. M. Ajayan, Evolution of the electronic band structure and efficient photo-detection in atomic layers of InSe, ACS Nano **8**, 1263 (2014).

[23] O. Del Pozo-Zamudio, S. Schwarz, J. Klein, R. C. Schofield, E. A. Chekhovich, O. Ceylan, E. Margapoti, A. I. Dmitriev, G. V. Lashkarev, D. N. Borisenko*et al.*, Photoluminescence and Raman investigation of stability of InSe and GaSe thin films. arxiv:1506.05619v, (2015).

[24] S. R. Tamalampudi, Y. Y. Lu, R. Kumar U, R. Sankar, C. D. Liao, K. M. B. C, H. Cheng, F. C. Chou, and Y. T. Chen, High performance and bendable Few-layered InSe photodetectors with broad spectral response, Nano Lett. **14**, 2800 (2014).

[25] J. Lauth, F. E. S. Gorris, M. S. Khoshkhoo, T. Chasse, W. Friedrich, V. Lebedeva, A. Meyer, C. Klinke, A. Kornowski, M. Scheele, and H. Weller, Solution-Processed Two-dimensional ultrathin InSe nanosheets, Chem. Mater. **28**, 1728 (2016).

[26] S. Sucharitakul, N. J. Goble, U. R. Kumar, R. Sankar, Z. A. Bogorad, F.-C. Chou, Y.-T. Chen, and X. P. A. Gao, Intrinsic electron mobility exceeding 10^3 $cm^2/(Vs)$ in multilayer InSe FETs, Nano Lett. **15**, 3815 (2015).

[27] G. Kresse and J. Furthmüller, Efficiency of ab-initio total energy calculations for metals and semiconductors using a plane-wave basis set, Comput. Mater. Sci. **6**, 15 (1996).

[28] P. E. Blöchl, Projector augmented-wave method, Phys. Rev. B **50**, 17953 (1994).

[29] J. Heyd, G. E. Scuseria, and M. Ernzerhof, Hybrid functionals based on a screened Coulomb potential, J. Chem. Phys. **118**, 18 (2003).

[30] Z. Xu, M. Chen, and S. F. Liu, Layer-dependent ultrahigh-mobility transport properties in all inorganic two-dimensional $Cs_2PbI_2Cl_2$ and $Cs_2SnI_2Cl_2$ perovskites, J. Phys. Chem. C **123**, 27978 (2019).

[31] J. Even, L. Pedesseau, J.-M. Jancu, and C. Katan, Importance of spin-orbit coupling in hybrid organic/inorganic perovskites for photovoltaic applications, J. Phys. Chem. Lett. **4**, 2999 (2013).

[32] S. Grimme, J. Antony, S. Ehrlich, and H. Krieg, A consistent and accurate ab initio parametrization of density functional dispersion correction (DFT-D) for the 94 elements H-Pu, J. Chem. Phys. **132**, 154104 (2010).

[33] K. Momma and F. Izumi, Vesta: A three-dimensional visual-ization system for electronic and structural analysis, J. Appl. Crystallogr. **41**, 653 (2008).

[34] M. X. Chen, W. Chen, Z. Zhang, and M. Weinert, Effects of magnetic dopants in $(Li_{0.8}M_{0.2}OH)FeSe$ (M=Fe, Mn, Co): Density functional theory study using a band unfolding technique, Phys. Rev. B **96**, 245111 (2017).

[35] M. Chen and M. Weinert, Layer k-projection and unfolding electronic bands at interfaces, Phys. Rev. B **98**, 245421 (2018).

[36] Y. Q. Zhao, Q. R. Ma, B. Liu, Z. L. Yu, J. Yang, and M. Q. Cai, Layer-dependent transport and optoelectronic property in two-dimensional perovskite: $(PEA)_2PbI_4$, Nanoscale **10**, 8677 (2018).

[37] X. Chen, J. Jiang, Q. Liang, R. Meng, C. Tan, Q. Yang, S. Zhang, and H. Zeng, Tunable electronic structure and enhanced optical properties in quasi-metallic hydrogenated/fluorinated SiC heterobilayer, J. Mater. Chem. C **4**, 7406 (2016).

[38] M. Gajdoš, K. Hummer, G. Kresse, J. Furthmüller, and F. Bechstedt, Linear optical properties in the projector-augmented wave methodology, Phys. Rev. B **73**, 045112 (2006).

[39] W. Luo, Y. Cao, P. Hu, K. Cai, Q. Feng, F. Yan, T. Yan, X. Zhang, and K. Wang, Gate tuning of high-performance InSe-based photodetectors using graphene electrodes, Adv. Opt. Mater. **3**, 1418 (2015).

[40] Y. M. Ding, J. J. Shi, C. Xia, M. Zhang, J. Du, P. Huang, M. Wu, H. Wang, Y.-L. Cen, and Shu-hang Pan, Enhancement of hole mobility in InSe monolayer via an InSe and black phosphorus heterostructure, Nanoscale **9**, 14682 (2017).

[41] S. Smidstrup, T. Markussen, P. Vancraeyveld, J. Wellendorff, J. Schneider, T. Gunst, B. Verstichel, D. Stradi, P. A. Khomyakov, and U. G. Vej-Hansen, Quantumatk: An integrated platform of electronic and atomic-scale modelling tools, J. Phys.: Condens. Matter. **32**, 015901 (2020).

[42] See the Supplemental Material at http://link.aps.org/supplemental/10.1103/PhysRevApplied.13.064053 for additional details, including various stacking configurations, the lattice constants, calculated effective mass, the work function, and the band structures.

[43] I. A. Kibirev, A. V. Matetskiy, A. V. Zotov, and A. A. Saranin, Thickness-dependent transition of the valence band shape from parabolic to Mexican-hat-like in the MBE

grown InSe ultrathin films, Appl. Phys. Lett. **112**, 191602 (2018).

[44] T. Shen, J. C. Ren, X. Liu, S. Li, and W. Liu, Van der Waals stacking induced transition from Schottky to Ohmic contacts: 2D metals on multilayer InSe, J. Am. Chem. Soc. **141**, 3110 (2019).

[45] Y. D. Zhou, Q. L. Liu, C. Yang, and Z. Y. Zhao, Interfacial micro-structure and properties of TiO_2/SnO_2 heterostructures with rutile phase: A DFT calculation investigation, Appl. Surf. Sci. **451**, 258 (2018).

[46] J. Shang, L. Pan, X. Wang, J. Li, H. X. Deng, and Z. Wei, Tunable electronic and optical properties of InSe/InTe van der Waals heterostructures toward optoelectronic applications, J. Mater. Chem. C **6**, 7201 (2018).

[47] S. Singh, Z. Zanolli, M. Amsler, B. Belhadji, J. O. Sofo, M. J. Verstraete, and A. H. Romero, Low-Energy phases of Bi monolayer predicted by structure search in Two dimensions, J. Phys. Chem. Lett. **10**, 7324 (2019).

[48] Noah F.Q. Yuan, Hiroki Isobe, and Liang Fu, Magic of high-order van hove singularity, Nat. Commun. **10**, 5769 (2019).

[49] G. Li, A. Luican, J. M. B, Lopes dos Santos, A. H. Castro Neto, A. Reina, J. Kong, and E. Y. Andrei, Observation of Van Hove singularities in twisted graphene layers, Nat. Phys. **6**, 109 (2010).

[50] D. I. Indolese, R. Delagrange, P. Makk, J. R. Wallbank, K. Wanatabe, T. Taniguchi, and C. Schönenberger, Signatures of van Hove Singularities Probed by the Supercurrent in a Graphene-hBN Superlattice, Phys. Rev. Lett. **121**, 137701 (2018).

[51] R. W. Havener, Yufeng Liang, L. Brown, L. Yang, and J. Park, Van Hove singularities and excitonic effects in the optical conductivity of twisted bilayer graphene, Nano Lett. **14**, 3353 (2014).

[52] P. Das, D. Wickramaratne, B. Debnath, G. Yin, and R. K. Lake, Charged impurity scattering in two-dimensional materials with ring-shaped valence bands: GaS, GaSe, InS, and InSe, Phys. Rev. B **99**, 085409 (2019).

[53] T. Cao, Z. Li, and S. G. Louie, Tunable Magnetism and Half-Metallicity in Hole-Doped Monolayer GaSe, Phys. Rev. Lett. **114**, 236602 (2015).

[54] J. Nitta, T. Akazaki, H. Takayanagi, and Takatomo Enoki, Gate Control of Spin-Orbit Interaction in an Inverted $In_{0.53}Ga_{0.47}As/In_{0.52}Al_{0.48}As$ Heterostructure, Phys. Rev. Lett. **78**, 1335 (1997).

[55] S. Singh and A. H. Romero, Giant tunable Rashba spin splitting in a two-dimensional BiSb monolayer and in BiSb/AlN heterostructures, Phys. Rev. B **95**, 165444 (2017).

[56] Z. Zhong, A. Toth, and K. Held, Theory of spin-orbit coupling at $LaAlO_3/SrTiO_3$ interfaces and $SrTiO_3$ surfaces, Phys. Rev. B **87**, 161102 (2013).

[57] A. D. Caviglia, M. Gabay, S. Gariglio, N. Reyren, C. Cancellieri, and J.-M. Triscone, Tunable Rashba Spin-Orbit Interaction at Oxide Interfaces, Phys. Rev. Lett. **104**, 126803 (2010).

[58] É. I. Rashba, Properties of semiconductors with an extremum loop. I. Cyclotron and combinational resonance in a magnetic field perpendicular to the plane of the loop, Sov. Phys. Solid State **2**, 1109 (1960).

[59] D. D. Sante, P. Barone, R. Bertacco, and S. Picozzi, Electric control of the giant rashba effect in bulk GeTe, Adv. Mater. **25**, 509 (2013).

[60] L.-B. Shi, S. Cao, M. Yang, Q. You, K.-C. Zhang, Y. Bao, Y.-J. Zhang, Y.-Y. Niu, and P. Qian, Theoretical prediction of intrinsic electron mobility of monolayer InSe: First-principles calculation, J. Phys.: Condens. Matter. **32**, 6 (2019).

[61] Y. Q. Zhao, X. Wang, B. Liu, Z. L. Yu, P. B. He, Q. Wan, M. Q. Cai, and H. L. Yu, Geometric structure and photovoltaic properties of mixed halide germanium perovskites from theoretical view, Org. Electron. **53**, 50 (2018).

[62] Z. L. Yu, Q. R. Ma, B. Liu, Y. Q. Zhao, L. Z. Wang, H. Zhou, and M. Q. Cai, Oriented tuning the photovoltaic properties of γ-$RbGeX_3$ by strain-induced electron effective mass mutation, J. Phys. D: Appl. Phys. **50**, 465101 (2017).

[63] B. Liu, M. Q. Long, M. Q. Cai, and J. L. Yang, Influence of the number of layers on ultrathin $CsSnI_3$ perovskite: From electronic structure to carrier mobility, J. Phys. D: Appl. Phys. **51**, 105101 (2018).

[64] B. Liu, L. J. Wu, Y. Q. Zhao, L. Z. Wang, and M. Q. Cai, The interfacial properties of $SrRuO_3/MoS_2$ heterojunction: A first-principles study, Eur. Phys. J. B **89**, 80 (2016).

[65] D. Cao, B. Liu, H. L. Yu, W. Y. Hu, and M. Q. Cai, First-principles study of electronic and magnetic properties in Co doped $BaTiO_3$, Eur. Phys. J. **88**, 75 (2015).

[66] D. Cao, B. Liu, H. L. Yu, W. Y. Hu, and M. Q. Cai, Critical thickness for ferroelectricity and magnetoelectric effect in multiferroic tunnel junction with symmetrical and asymmetrical electrodes, Eur. Phys. J. B **86**, 504 (2013).

[67] M. Q. Cai, Y. Du and B, and Y. Huang, First-principles study of the critical thickness in asymmetric ferroelectric tunnel junctions, Appl. Phys. Lett. **98**, 102907 (2011).

[68] D. Cao, M. Q. Cai, W. Y. Hu, J. Peng, Y. Zheng, and H. T. Huang, Uniaxial strain-modulated conductivity in manganit superlattice ($LaMnO_3/SrMnO_3$), Appl. Phys. Lett. **98**, 031910 (2011).

[69] D. Cao, M. Q. Cai, W. Y. Hu, and C. M. Xu, Magnetoelectric effect and critical thickness for ferroelectricity in $Co/BaTiO_3/Co$ multiferroic tunnel junctions, J. Appl. Phys. **109**, 114107 (2011).

[70] B. Liu, L. J. Wu, Y. Q. Zhao, L. Z. Wang, and M. Q. Cai, A first-principles study of magnetic variation via doping vacancy in monolayer VS_2, J. Magn. Magn. Mater. **420**, 218 (2016).

[71] D. J. Yang, Y. H. Du, Y. Q. Zhao, Z. L. Yu, and M. Q. Cai, Interfacial interactions and enhanced optoelectronic properties in $CsSnI_3$-black phosphorus van der waals heterostructures, Phys. Status Solidi b **256**, 1800540 (2019).

[72] C. S. Liao, Q. Q. Zhao, Y. Q. Zhao, Z. L. Yu, P. B. Be, J. L. Yang, and M. Q. Cai, First-principles investigations of electronic and optical properties in the $MoS_2/CsPbBr_3$ heterostructure, J. Phys. Chem. Solids **135**, 109060 (2019).

[73] Z. L. Yu, Y. Q. Zhao, P. B. He, B. Liu, J. L. Yang, and M. Q. Cai, The influence of electrode for electroluminescence devices based on all-inorganic halide perovskite, J. Phys.: Condens. Matter **32**, 065002 (2020).

[74] Z. L. Yu, Y. Q. Zhao, Q. Wan, B. Liu, J. L. Yang, and M. Q. Cai, Theoretical study on the effect of the optical properties and electronic structure for the Bi-doped $CsPbBr_3$, J. Phys.: Condens. Matter. **32**, 205504 (2020).